

1 **Simulations of Energetic Neutral Atom sputtering from**  
2 **Ganymede in preparation for the JUICE mission**

3 **A. Pontoni<sup>1</sup>, M. Shimoyama<sup>1</sup>, Y. Futaana<sup>1</sup>, S. Fatemi<sup>2</sup>, A. R. Poppe<sup>3</sup>, M.**  
4 **Wieser<sup>1</sup>, S. Barabash<sup>1</sup>**

5 <sup>1</sup>Swedish Institute of Space Physics, Kiruna, Sweden

6 <sup>2</sup>Department of Physics at Umeå University, Umeå, Sweden

7 <sup>3</sup>Space Sciences Laboratory, University of California, Berkeley, CA, USA

8 **Key Points:**

- 9
- 10 • A new method for calculating sputtered fluxes at Ganymede is introduced
  - 11 • The energy spectra of sputtered H<sub>2</sub>O, O<sub>2</sub>, and H<sub>2</sub> ENAs are calculated for the first  
12 time
  - 13 • The Jovian Neutrals Analyzer on JUICE can remotely map ion precipitation at  
Ganymede

---

Corresponding author: Angèle Pontoni, [angele.pontoni@irf.se](mailto:angele.pontoni@irf.se)

**Abstract**

Jovian magnetospheric plasma irradiates the surface of Ganymede and is postulated to be the primary agent that changes the surface brightness of Ganymede, leading to asymmetries between polar and equatorial regions as well as between the trailing and leading hemispheres. As impinging ions sputter surface constituents as neutrals, ion precipitation patterns can be remotely imaged using the Energetic Neutral Atoms (ENA) measurement technique. Here we calculate the expected sputtered ENA flux from the surface of Ganymede to help interpret future observations by ENA instruments, particularly the Jovian Neutral Analyzer (JNA) onboard the JUpiter ICy moon Explorer (JUICE) spacecraft. We use sputtering models developed based on laboratory experiments to calculate sputtered fluxes of  $\text{H}_2\text{O}$ ,  $\text{O}_2$ , and  $\text{H}_2$ . The input ion population used in this study is the result of test particle simulations using electric and magnetic fields from a hybrid simulation of Ganymede's environment. This population includes a thermal component ( $\text{H}^+$  and  $\text{O}^+$  from 10 eV to 10 keV) and an energetic component ( $\text{H}^+$ ,  $\text{O}^{++}$  and  $\text{S}^{+++}$  from 10 keV to 10 MeV). We find a global ENA sputtering rate from Ganymede of  $1.42 \times 10^{27} \text{ s}^{-1}$ , with contributions from  $\text{H}_2$ ,  $\text{O}_2$ , and  $\text{H}_2\text{O}$  of 34%, 17%, and 49% respectively. We also calculate the energy distribution of sputtered ENAs, give an estimate of a typical JNA count rate at Ganymede, and investigate latitudinal variations of sputtered fluxes along a simulated orbit track of the JUICE spacecraft. Our results demonstrate the capability of the JNA sensor to remotely map ion precipitation at Ganymede.

**Plain Language Summary**

Particles trapped by Jupiter's magnetic field interact with Jupiter's moons. Ganymede, the largest of those moons, lacks a dense atmosphere to protect its surface from these energetic Jovian particles, but Ganymede's magnetic field is strong enough to influence their trajectory: charged particles are deflected away from equatorial regions to polar regions, resulting in uneven particle precipitation patterns at the surface of Ganymede. When ions hit the surface of Ganymede, they eject particles from the surface, in a process referred to as sputtering. Those particles are mostly neutral and therefore unaffected by Ganymede's magnetic fields, so we can image where ions hit the surface of Ganymede by measuring ejected neutral particles. The Jovian Neutrals Analyzer (JNA) will fly onboard the JUpiter ICy moon Explorer (JUICE) spacecraft and will measure sputtered neutrals in the vicinity of Ganymede. To help interpret the data to be collected by JNA, we used models derived from laboratory experiments to simulate what JNA will observe at Ganymede. Our results show that JNA will be able to show us where ions hit the surface of Ganymede, which is important as uneven ion precipitation is thought to explain why Ganymede's poles are brighter than its equatorial regions.

## 1 Introduction

Imaging plasma precipitation patterns at the surface of Ganymede is a key measurement for understanding the effect of Jovian plasma precipitation on the brightness and composition of the surface. Ganymede stands out as Jupiter's largest moon and also the only moon in the Solar System to feature an intrinsic magnetic field, causing the formation of a small magnetosphere inside Jupiter's much larger magnetosphere. Ganymede's magnetic field locally impedes or enhances Jovian plasma access to its surface, resulting in variable precipitation patterns (Khurana et al., 2007; Fatemi et al., 2016; Poppe et al., 2018; Plainaki et al., 2020a). Precipitating ions can be backscattered by the surface or cause surface constituents and radiolytic products to sputter. Backscattered and sputtered particles leave the surface mainly as neutral and with energies ranging from eV to MeV (Johnson, 1990).

Such neutral particles are usually referred to as Energetic Neutral Atoms (ENAs) (Gruntman, 1997). ENAs are well-known populations in the terrestrial magnetosphere (Roelof, 1987). They originate from ions neutralized by charge-exchange with neutrals, and are used to probe distant plasma in space. The trajectories of ENAs are not influenced by electric or magnetic fields and therefore preserve information about their original velocity, assuming that the gravitational force is negligible. Thus ENA measurements can and have been used to remotely map ion precipitation on airless bodies, where in-situ precipitating ion observation is not easily possible. For example, backscattered solar wind protons and sputtered oxygen atoms were observed at the Moon by the Interstellar Boundary EXplorer (IBEX) (McComas et al., 2009; Allegrini et al., 2013) and by CENA on Chandrayaan-1 (Wieser et al., 2016; Vorburger et al., 2014; Futaana et al., 2013). Ganymede will also be visited by an ENA instrument: the Jovian Neutrals Analyzer (JNA) will fly on-board the JUPITER ICY moon Explorer (JUICE) spacecraft.

To help interpret the data collected by JNA, estimates of ENA fluxes are needed. However, estimating ENA fluxes requires modelling the sputtering process. The sputtering process has been widely studied because of its relevance for icy bodies such as Ganymede, Europa, and Enceladus. Their lack of a dense atmosphere leaves their surface exposed to ion precipitation, leading to the sputtering of surface constituents and radiolytic products. Along with other processes such as sublimation and photo-stimulated desorption, sputtering contributes to the creation of a neutral exosphere on several bodies (Cooper, 2001; Johnson et al., 2004; Marconi, 2007; Cassidy et al., 2010; Wurz et al., 2010).

While a comprehensive analytical description of the sputtering process is not currently available, sputtering has been extensively studied through laboratory experiments (Baragiola et al., 2003; Famá et al., 2008; Teolis et al., 2017; Galli et al., 2017, 2018). Several methods have been developed to calculate the sputtering yield of ions on icy surfaces as a function of projectile energy and species, incidence angle, and surface temperature (Johnson et al., 2004; Famá et al., 2008; Teolis et al., 2017). Such methods, or combinations of them, have been used extensively to simulate surface-plasma interactions at Europa (Vorburger & Wurz, 2018; Plainaki et al., 2010, 2012) and Ganymede (Marconi, 2007; Turc et al., 2014; Plainaki et al., 2015; Shematovich, 2016; Leblanc et al., 2017; Poppe et al., 2018; Plainaki et al., 2020a).

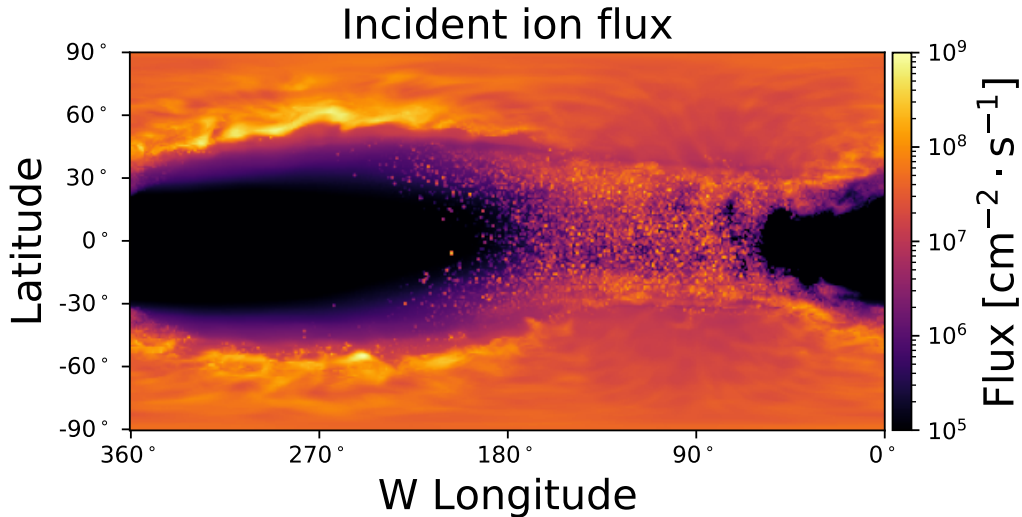
Here, we estimate sputtered ENA fluxes at the surface of Ganymede by applying models formulated by Famá et al. (2008), Johnson et al. (2004) and Teolis et al. (2017) to a population of incident Jovian plasma obtained through hybrid simulations by Poppe et al. (2018). This allows us to calculate the expected sputtered ENA fluxes of H<sub>2</sub>O, H<sub>2</sub>, and O<sub>2</sub> and to further apply the Thompson-Sigmund law expressed in Vorburger and Wurz (2018) to calculate their energy distribution. By convolving JNA's estimated geometric factor with the energy distribution, we give an expected JNA count rate in the vicinity of Ganymede. Finally we investigate latitudinal variations of the sputtered ENA fluxes by simulating a simplified orbit of the JUICE spacecraft around Ganymede.

## 2 Materials and Methods

### 2.1 Input population

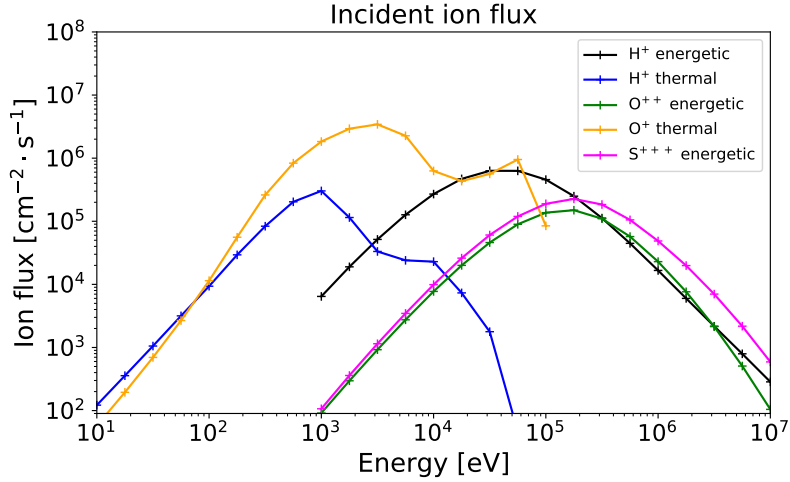
The incident ion population is taken from a combination of three-dimensional hybrid simulations of Ganymede’s magnetosphere and subsequent backwards-Liouville particle tracing through the hybrid electromagnetic fields (Fatemi et al., 2016; Poppe et al., 2018). They simulated the ion velocity distribution for the Galileo G8 flyby, when Ganymede was in the Jovian plasma sheet. The incident population used as an input for calculating the sputtered ENA flux in this study is comprised of three-dimensional velocity distribution functions for thermal  $O^+$  and  $H^+$  from 10 eV to 10 keV and energetic  $H^+$ ,  $O^{++}$  and  $S^{+++}$  from 10 keV to 10 MeV. The spatial resolution of the hybrid model is  $1^\circ \times 1^\circ$  in latitude and longitude at the surface of Ganymede.

Figure 1 shows the resulting plasma precipitation pattern, i.e. a map of the ion flux integrated over all incident species, energies and angles. On the trailing hemisphere ( $180^\circ - 360^\circ W$ ) of the equatorial regions, Ganymede’s surface is shielded from Jovian plasma by Ganymede’s intrinsic magnetic field. In contrast, intense precipitation is observed on the leading hemisphere of the equatorial regions ( $0^\circ - 180^\circ W$ ), where plasma is accelerated back towards Ganymede by reconnection in the magnetotail (Fatemi et al., 2016; Poppe et al., 2018). The most intense flux is observed in the high-latitude cusp regions on the leading hemisphere, where open-closed magnetic field lines boundaries are located ( $\pm 50^\circ - 60^\circ$  in latitude) (Poppe et al., 2018).



**Figure 1.** Incident ion flux at the surface of Ganymede, taken from Poppe et al. (2018) and integrated over all species, angles and energies. The leading hemisphere extends from  $0^\circ W$  to  $180^\circ W$  while the trailing hemisphere extends from  $180^\circ W$  to  $360^\circ W$ . For our study here, we choose a single period along Ganymede’s orbit such that the sub-solar point is located at  $270^\circ W$ , i.e. the co-rotating plasma flow is aligned with the sunlight direction.

Figure 2 shows the energy distribution of the incident ion flux at Ganymede’s surface resulting from Poppe’s backwards-Liouville tracing model. The flux was integrated over all incident angles and averaged over the surface of Ganymede. Two components can be identified: i) the thermal component comprised of plasma from Io’s torus diffusing outwards (Siscoe & Summers, 1981); ii) the energetic component originating from accelerated Io torus plasma and solar wind plasma diffusing inwards (Siscoe et al., 1981).



**Figure 2.** Energy spectra of the precipitating ions used as our input ion populations, integrated over all incident angles and averaged over the surface of Ganymede.

128

## 2.2 Sputtering yield

129

130

131

132

133

134

135

136

137

138

Ion sputtering on water ice has been extensively studied via laboratory experiments and the sputtered products are known to be comprised of  $\text{H}_2\text{O}$ ,  $\text{H}_2$ , and  $\text{O}_2$  (Johnson et al., 2004; Galli et al., 2017). While  $\text{H}_2\text{O}$  is a surface constituent directly sputtered by the impact of ions on water ice,  $\text{H}_2$  and  $\text{O}_2$  are radiolytic products generated in the material by the irradiation of water ice and subsequently sputtered by projectiles (Johnson et al., 2003; Paranicas et al., 2009; Teolis et al., 2017). Here we use three different functions to calculate the sputtering yield, depending on the energy of the incident ions and the sputtered species. Throughout the paper, the sputtering yield of a sputtered species *by* an incident species refers to the number of particles of the sputtered species released from the surface by one incident ion.

139

140

141

At incident ion energies higher than 100 keV, we use the model described in Johnson et al. (2004) to calculate  $Y_{\text{H}_2\text{O},\text{high}}$ , the yield of  $\text{H}_2\text{O}$  as a function of the energy and species of the incident ion:

142

$$\frac{1}{Y_{\text{H}_2\text{O},\text{high}}(v, Z)} = \frac{1}{11.2 Z^{2.8} (v/Z^{1/3})^{-2.24}} + \frac{1}{4.2 Z^{2.8} (v/Z^{1/3})^{2.16}}, \quad (1)$$

143

144

where  $Z$  is the atomic number of the incident particle and  $v$  the velocity of the incident particle in atomic units ( $1 \text{ au} = 2.18 \cdot 10^8 \text{ cm} \cdot \text{s}^{-1}$ ).

145

146

147

At incident ion energies lower than 100 keV, we use the model described in Famá et al. (2008) to calculate  $Y_{\text{H}_2\text{O},\text{low}}$ , the yield of  $\text{H}_2\text{O}$  as a function of the energy, species, and incident angle of the incident particle:

148

$$Y_{\text{H}_2\text{O},\text{low}}(E, m, Z, \beta) = \frac{1}{U_0} \left( \frac{3}{4\pi^2 C_0 \alpha S_n} + \eta S_e^2 \right) \cos^{-f}(\beta), \quad (2)$$

149

150

151

152

153

154

where  $E$ ,  $m$ , and  $Z$  are respectively the energy, mass, and atomic number of the projectile.  $\beta$  is the incidence angle, defined from the surface normal. At low-energies, where elastic sputtering processes dominate, the yield is inversely proportional to the nuclear-stopping cross section  $S_n$ . At high energies, where electronic processes dominate, the yield is proportional to the squared electronic-stopping cross section  $S_e$ . Details about the other constants ( $U_0$ ,  $C_0$ ,  $\alpha$ ,  $\eta$ , and  $f$ ) can be found in Famá et al. (2008).

155 In eq. 2 we do not include the temperature-dependent component of Famá's model,  
 156 as it is attributed to H<sub>2</sub> and O<sub>2</sub> produced by radiolysis, a temperature-dependent pro-  
 157 cess. Instead, we calculate the yield of H<sub>2</sub> ( $Y_{H_2}(E, T, \beta)$ ) and that of O<sub>2</sub> ( $Y_{O_2}(E, T, \beta)$ )  
 158 using the model derived by Teolis et al. (2017):

$$Y_{O_2}(E, T, \beta) = \frac{Y_{H_2}(E, T, \beta)}{2} = \epsilon g_{O_2}^0 x_o \left[ 1 - \exp\left(-\frac{r_o \cos(\beta)}{x_o}\right) \right] \left[ 1 + q_o \exp\left(-\frac{Q}{k_b T}\right) \right] / r_o \cos(\beta), \quad (3)$$

160 where  $T$  is the temperature of the surface of Ganymede,  $\beta$  the incidence angle of the pro-  
 161 jectile measured from the surface normal, and  $k_b$  is the Boltzmann constant. Details about  
 162  $\epsilon$ ,  $g_{O_2}^0$ ,  $x_o$ ,  $r_o$ ,  $q_o$ , and  $Q$  can be found in Teolis et al. (2017). The temperature model  
 163 used in this study was derived by Marconi (2007) based on data from the Galileo space-  
 164 craft (Orton et al., 1996). The dayside temperature is given by  $T(\lambda) = 70 \cos(\lambda)^{0.75} +$   
 165 80 K (where  $\lambda$  is the sub-solar latitude) and the nightside temperature is a constant 80  
 166 K.

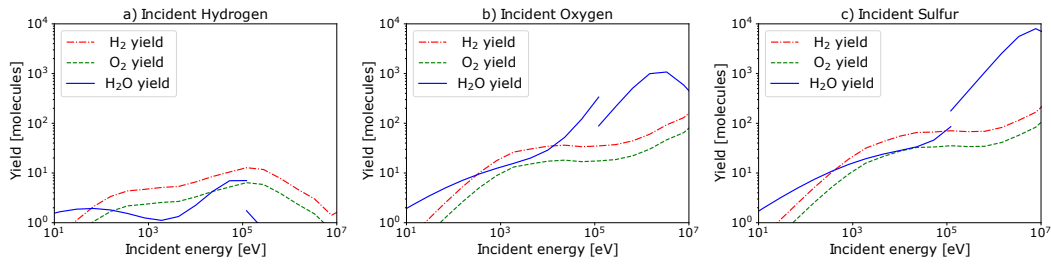


**Figure 3.** Sputtering yield of H<sub>2</sub>O, H<sub>2</sub> and O<sub>2</sub> by incident a) H, b) O, and c) S ions. The discontinuity at 100 keV for the H<sub>2</sub>O yields is explained by the transition of the model from Famá's to Johnson's. The yields of H<sub>2</sub> and O<sub>2</sub> are calculated using only Teolis' model.

167 Figure 3 shows the sputtering yield of H<sub>2</sub>O, O<sub>2</sub> and H<sub>2</sub> by O, H and S ions imping-  
 168 ing on water ice. The discontinuity at 100 keV for the H<sub>2</sub>O yields is due to the transi-  
 169 tion of the model from Famá's to Johnson's. We chose 100 keV as the threshold for the  
 170 transition based on work by Cassidy et al. (2013a), but our results are not sensitive to  
 171 the threshold energy. Generally, the H<sub>2</sub>O yield by O and S is higher than 1 and increases  
 172 with energy for most of the energy range shown here. Because of its low atomic mass,  
 173 the yield by H is much lower. A surface temperature of 124 K was used to generate these  
 174 figures, which corresponds to an average daytime disk temperature (Grundy et al., 1999).  
 175 As mentioned above, the actual surface temperature used in our model varies between  
 176 80 K on the nightside and 150 K at the sub-solar point.

### 177 2.3 Sputtered energy distribution

178 We assume a Thompson-Sigmund law to calculate the probability distribution  $S(K)$   
 179 of the energy of the sputtered particles, expressed in (Vorburger & Wurz, 2018) as:

$$S(K) = \frac{6E_b}{3 - 8\sqrt{K/E_i}} \frac{K}{(K + E_b)^3} \cdot \left( 1 - \sqrt{\frac{K + E_b}{4E_i(M_1M_2)/(M_1 + M_2)^2}} \right), \quad (4)$$

181 where  $K$  is the energy of the sputtered neutral particle,  $E_b$  the binding energy of the sur-  
 182 face (0.054 eV as also used in Plainaki et al. (2015)),  $E_i$  the energy of the projectile, and  
 183  $M_1$  and  $M_2$  are the masses of the projectile and sputtered neutral particle.

184 Figure 4a shows the energy distribution of H<sub>2</sub>O molecules sputtered by H, O and  
 185 S with an incident energy of 100 keV. The main consequence of the difference in atomic

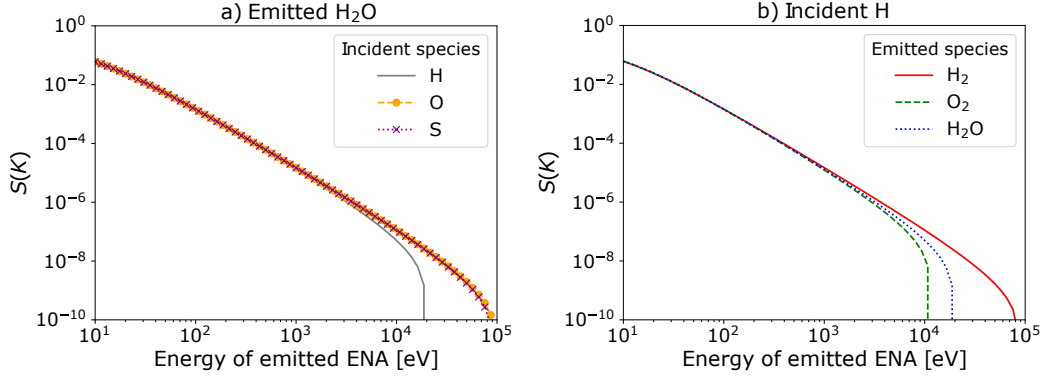


**Figure 4.** a) Probability distribution of the energy of H<sub>2</sub>O sputtered by different incident species. b) Probability distribution of the energy of H<sub>2</sub>O, H<sub>2</sub> and O<sub>2</sub> molecules sputtered by H, for incident energies of 100 keV.

186 mass is the cutoff energy of sputtered particles: sputtered H has a cutoff energy of about  
 187 20 keV, much lower than the cutoff energy of heavier oxygen and sulfur at about 90 keV.  
 188 Figure 4b shows the energy distribution of H<sub>2</sub>O, H<sub>2</sub> and O<sub>2</sub> molecules sputtered by 100  
 189 keV H. Higher masses result in lower cutoff energies, with respective cutoff energies for  
 190 O<sub>2</sub>, H<sub>2</sub>O, and H<sub>2</sub> of about 10 keV, 20 keV, and 80 keV.

## 191 2.4 Flux calculation

192 The differential flux of the sputtered neutrals,  $j(K)$ , is calculated from the com-  
 193 bination of the above-mentioned parameters, where  $K$  is the energy of the sputtered par-  
 194 ticle. In our model, the incident plasma taken from hybrid simulations is  $f(v, \theta, \phi)$ , in  
 195 units of  $(\text{m/s})^{-3} \text{sr}^{-1} \text{cm}^{-2} \text{s}^{-1}$ , for each bin at the surface (Poppe et al., 2018), where  $v$   
 196 is the incident velocity,  $\theta$  the incident elevation, and  $\phi$  the incident azimuth.

197 The differential flux  $j(K)$  (in units  $\text{cm}^{-2} \text{s}^{-1} \text{sr}^{-1} \text{eV}^{-1}$ ) is calculated using the fol-  
 198 lowing expression:

$$199 \quad j(K) = \frac{1}{2\pi} \int_v \int_\theta \int_\phi f(v, \theta, \phi) Y(E_i) S(K; E_i) v^2 \cos(\alpha) \sin(\theta) \, dv d\theta d\phi, \quad (5)$$

200 where  $E_i$  the energy of the incident species,  $Y(E_i)$  the sputtering yield function,  $S(K; E_i)$   
 201 the Thompson-Sigmund probability distribution function, and  $\alpha$  is the angle between  
 202 the velocity vector and the local normal vector pointing inward to the center of Ganymede  
 203 at the corresponding latitude and longitude. We assume that sputtered neutrals are ejected  
 204 isotropically and therefore divide the flux by  $2\pi$  to get the flux per solid angle.

## 205 3 Results

### 206 3.1 ENA sputtering maps

207 Figure 5 shows the calculated flux maps of the sputtered ENAs (H<sub>2</sub>, O<sub>2</sub>, and H<sub>2</sub>O)  
 208 integrated over all incident species, incident angles, and energies. The colorbar ranges  
 209 from  $10^6$  to  $10^{10} \text{ cm}^{-2} \cdot \text{s}^{-1}$  for all three maps. H<sub>2</sub> and O<sub>2</sub> fluxes are about 5 times higher  
 210 on the dayside than on the nightside due to the higher surface temperature on the day-  
 211 side, which results in a higher yield of H<sub>2</sub> and O<sub>2</sub> (eq. 3). As the yield of H<sub>2</sub>O is inde-  
 212 pendent of temperature, no significant difference between the dayside and the nightside  
 213 is observed other than that resulting from the input ion precipitation patterns.

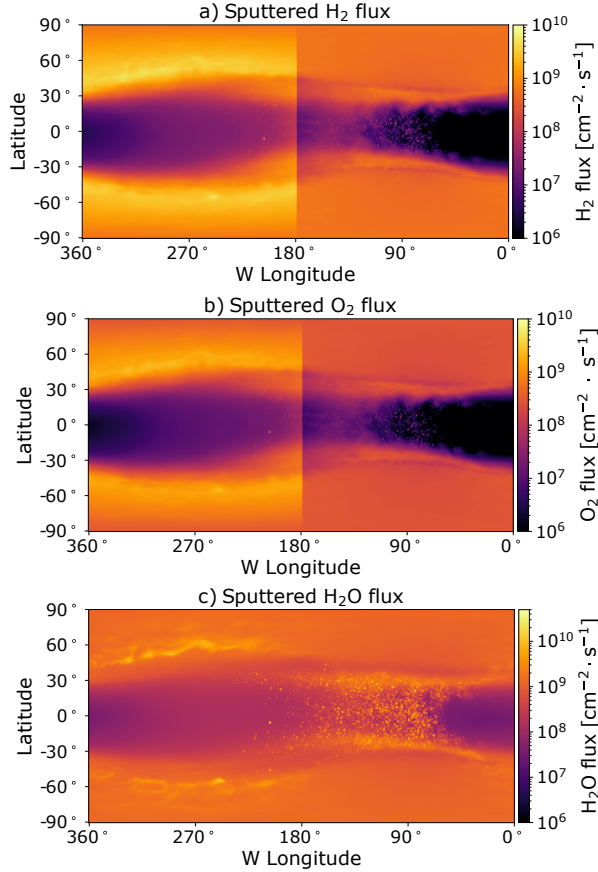


**Figure 5.** Maps of the sputtered fluxes of  $\text{H}_2$ ,  $\text{O}_2$  and  $\text{H}_2\text{O}$ , integrated over all incident species, energies, and angles.

214 Generally, similar patterns to the ion precipitation map (Figure 1) are observed for  
 215 ENA sputtering. Indeed, the sputtered ENA flux is higher in the polar regions than in  
 216 the equatorial regions, and the difference in ENA fluxes between the pole and the equator  
 217 is more distinct in the trailing hemisphere. The similarity between ion precipitation  
 218 patterns and sputtering rate patterns illustrates the relevance of the ENA imaging method  
 219 to remotely map ion precipitation at Ganymede, as previously shown for terrestrial bod-  
 220 ies (Futaana et al., 2006; Vorburger et al., 2014; Wieser et al., 2009; Allegrini et al., 2013;  
 221 Futaana et al., 2013).

222 However, we note an extra feature of the sputtered  $\text{H}_2\text{O}$  flux, observed in neither  
 223 the incoming ion flux pattern nor for sputtered  $\text{H}_2$  and  $\text{O}_2$ . At equatorial regions on the  
 224 leading side, the  $\text{H}_2\text{O}$  flux shows significant enhancement, with fluxes of the same order  
 225 as on the trailing side at the open-close field line boundaries. This enhancement contrasts  
 226 with the ion flux pattern: at equatorial regions on the leading side, the ion flux is atten-  
 227 uated compared to high-intensity precipitation regions around the open-close field line  
 228 boundaries. The discrepancy is likely due to the fact that while the ion flux is atten-  
 229 uated, it is also shifted to higher energies. High energy ions sputter more particles per in-  
 230 cident ion and are more efficient at sputtering  $\text{H}_2\text{O}$  than  $\text{H}_2$  and  $\text{O}_2$ . This results in  $\text{H}_2\text{O}$   
 231 fluxes at equatorial regions on the leading side comparable with  $\text{H}_2\text{O}$  fluxes at the open-  
 232 close field line boundaries on the trailing side.

### 3.2 Sputtered energy distribution

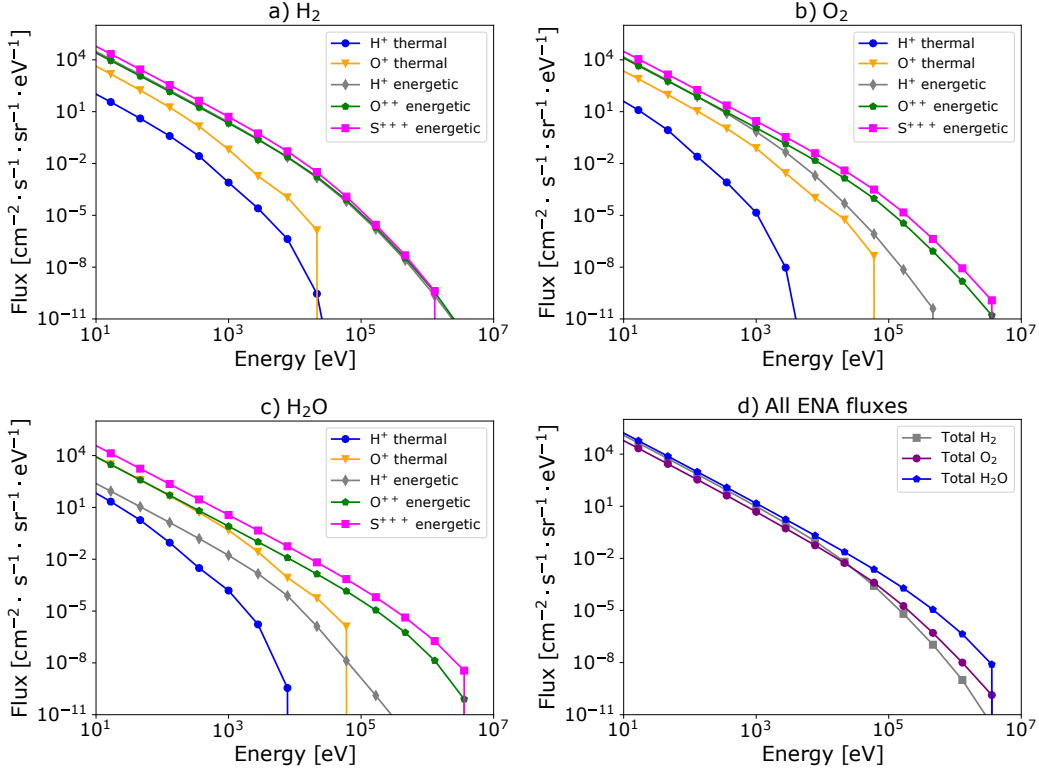


**Figure 6.** Globally averaged energy distributions of sputtered a)  $\text{H}_2$ , b)  $\text{O}_2$ , and c)  $\text{H}_2\text{O}$ , integrated over incident angles and energies. Different colors indicate the incident species which sputtered these ENAs. d) Energy distribution of all sputtered species, summed over incident species.

Figure 6 shows the energy spectra of sputtered  $\text{H}_2\text{O}$ ,  $\text{H}_2$ , and  $\text{O}_2$ . Because of the Thompson-Sigmund law (eq. 4) for the energy of sputtered ENAs, fluxes fall as energy increases. Although the incident ion population is dominated by the thermal  $\text{O}^+$  component at low energies, the contribution of energetic  $\text{S}^{+++}$  ions to the sputtered  $\text{H}_2\text{O}$ ,  $\text{H}_2$ , and  $\text{O}_2$  ENA fluxes dominates over that of all other species across the entire energy range. This is likely a combined effect of the heavier mass of  $\text{S}^{+++}$  ions, resulting in high sputtering yields, and the fact that the energy distribution of  $\text{S}^{+++}$  is skewed towards higher energies.

The lowest contribution to sputtered ENAs comes from the thermal  $\text{H}^+$  ion component because of their low incident flux (Figure 2) and low sputtering yield, lower than 10 across most of the energy range. For the same reason, energetic  $\text{H}^+$  ions contribute the least out of the three energetic species to sputtering  $\text{O}_2$  and  $\text{H}_2\text{O}$ . Energetic  $\text{H}^+$  ions sputter less  $\text{H}_2\text{O}$  molecules than thermal  $\text{O}^+$  ions up to 20 keV. At 20 keV,  $\text{H}_2\text{O}$  ENAs sputtered by  $\text{O}^+$  cut off, due to  $\text{O}^+$  ions being heavier than  $\text{H}^+$  and also contributing more to the incident ion flux.

Total sputtered fluxes of  $\text{H}_2\text{O}$ ,  $\text{H}_2$ , and  $\text{O}_2$  are compared with one another in Figure 6d)  $\text{H}_2\text{O}$  fluxes dominate over  $\text{H}_2$  and  $\text{O}_2$  over the entire spectrum, as reflected in the global sputtering rates calculated in section 3.3.

252

### 3.3 Total sputtering rate

253

254

255

256

257

258

259

By integrating the sputtered ENA flux over energy and the entire surface we obtain global sputtering rates of  $4.8 \times 10^{26}$ ,  $2.4 \times 10^{26}$  and  $7.0 \times 10^{26}$  molecules per second for  $\text{H}_2$ ,  $\text{O}_2$ , and  $\text{H}_2\text{O}$  respectively. This results in a total sputtering rate of  $1.42 \times 10^{27}$  molecules per second. Table 1 shows a comparison of our estimated sputtering rate with previous works. Given from left to right are the model reference, the input plasma model type (MHD or hybrid), the sputtering model(s), the energy range of the sputtered molecules, the species of the sputtered molecules, and the total sputtering rate.

**Table 1.** Total sputtering rate from the surface of Ganymede estimated by previously published works as well as this one.

Reference	Input	Sputtering models	Energy range	Sputtered species	Total sputtering rate [ $\text{s}^{-1}$ ]
Plainaki et al., 2015	MHD <sup>1</sup>	Famá <sup>3</sup>	1-100 keV	$\text{H}_2\text{O}$ , $\text{O}_2$	$6.94 \times 10^{25}$
Poppe et al., 2018	Hybrid <sup>2</sup>	Johnson <sup>4</sup>	10 eV - 10 MeV	$\text{H}_2\text{O}$	$7.5 \times 10^{26}$
Carnielli et al., 2020	MHD <sup>1</sup>	Famá <sup>3</sup> , Johnson <sup>4</sup>	1 eV - 30 MeV	$\text{H}_2\text{O}$	$2.25 \times 10^{27}$
This work	Hybrid <sup>2</sup>	Famá <sup>3</sup> , Johnson <sup>4</sup> , Teolis <sup>5</sup>	10 eV - 10 MeV	$\text{H}_2\text{O}$ , $\text{O}_2$ $\text{H}_2$	$1.42 \times 10^{27}$

<sup>1</sup> Jia et al. (2008)

<sup>2</sup> Fatemi et al. (2016)

<sup>3</sup> Famá et al. (2008)

<sup>4</sup> Johnson et al. (2004)

<sup>5</sup> Teolis et al. (2017)

260

261

262

263

264

265

266

All works give similar results within two orders of magnitude. The difference between our result and those of previous works can be qualitatively explained as follows. Plainaki et al. (2015) derived their ion population using electric and magnetic fields obtained with MHD simulations by Jia et al. (2008). Their energy range covered only 1-100 keV, which is narrower than in this study, leading to a total sputtering rate one order of magnitude lower than ours. They used Famá's model to calculate the yield of  $\text{H}_2\text{O}$  and  $\text{O}_2$ , but did not account for the sputtering of  $\text{H}_2$ .

267

268

269

270

271

272

Poppe et al. (2018), when they published the results of the hybrid simulation of Jovian plasma which were used in this study, took the opportunity to estimate the  $\text{H}_2\text{O}$  ENA sputtering rate using Johnson's model. However, at incident energies lower than 100 keV, Johnson's model underestimates the yield, which is better reproduced by Famá's (Cassidy et al., 2013b). Moreover, Poppe et al. (2018) considered only the sputtering of  $\text{H}_2\text{O}$ , whereas we considered  $\text{O}_2$  and  $\text{H}_2$  in addition to  $\text{H}_2\text{O}$ .

273

274

275

276

277

278

Carnielli et al. (2020) used the model in Jia et al. (2008) also used to derive their input ion population, but considered energies ranging from 1 eV to 30 MeV, a wider energy range than used here. Moreover, they considered the contribution of Ganymede's ionospheric ions, which they showed can contribute to up to 10% of the ENA sputtering rate. Their ionospheric ion population was comprised of  $\text{O}_2^+$ ,  $\text{O}^+$ ,  $\text{H}_2\text{O}$ ,  $\text{H}_2^+$ ,  $\text{H}^+$ , and  $\text{OH}^+$  with energies ranging from 10 eV to 10 keV. As our input population did not in-

279 clude ionospheric ions and covered a narrower energy range, our total sputtering rate is  
 280 expected to be lower than theirs.

281 Our results suggest that H<sub>2</sub> and O<sub>2</sub> account for half of the total neutral sputter-  
 282 ing rate from the surface of Ganymede, showing that their contribution should be con-  
 283 sidered in addition to that of H<sub>2</sub>O.

### 284 3.4 JNA count rate estimation

285 The JUICE spacecraft, planned to launch in 2022 and expected to reach Jupiter  
 286 in the 2030s, carries the Particle Environment Package (PEP). PEP is comprised of six  
 287 sensors tailored to study how Jovian plasma interacts with Ganymede’s magnetosphere,  
 288 tenuous atmosphere, and icy surface. In particular, the Jovian Neutrals Analyzer (JNA)  
 289 will measure ENAs in the Jovian environment in the energy range between 10 eV to 3.3  
 290 keV, with a field-of-view of 15° in elevation and 150° in azimuth, divided into 11 pix-  
 291 els (Shimoyama et al., 2018). JNA takes heritage from the CENA instrument family (Kazama  
 292 et al., 2007; Barabash et al., 2009), and measures ENAs using: (1) a deflection/collimation  
 293 system that repels ions up to 9kV (2) a conversion surface for neutral to ion conversion  
 294 (3) a wave system for energy analysis (10 eV - 3.3 keV range with 100% energy resolu-  
 295 tion) (4) a Time-Of-Flight (TOF) cell that measures the velocity of the particle.

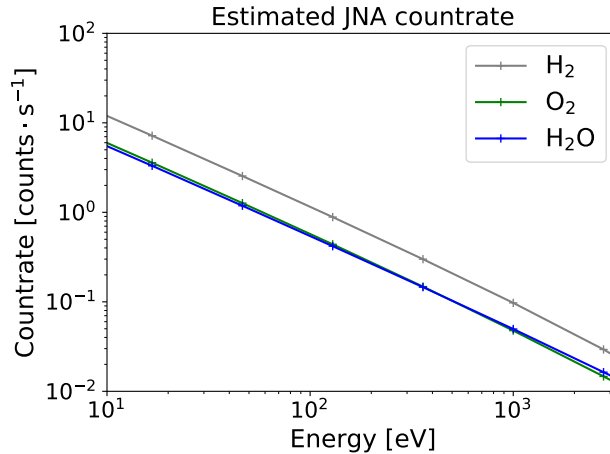


**Figure 7.** Simulated JNA count rate as a function of energy for sputtered H<sub>2</sub>O, O<sub>2</sub> and H<sub>2</sub> in the energy range JNA can measure.

296 Here we estimate the count rate that JNA is expected to observe at Ganymede by  
 297 multiplying the flux calculated in section 3.2 by JNA’s estimated geometric factor, GF =  
 298  $10^{-5} \text{ cm}^2 \cdot \text{sr} \cdot \text{eV}/\text{eV}$ . Figure 7 shows simulated JNA count rates as a function of en-  
 299 ergy. The geometric factor we used is constant across the energy range, so the count rate  
 300 distribution follows the Thompson-Sigmund law applied to the sputtered ENAs, result-  
 301 ing in count rates as high as  $10^1 \text{ counts} \cdot \text{s}^{-1}$  at 20 eV and as low as  $10^{-2} \text{ counts} \cdot \text{s}^{-1}$   
 302 at 3.3 keV. JNA is optimized to measure small fluxes, i.e. low count rates, even in the  
 303 harsh radiation environment expected at Jupiter. To achieve this, two Channel Electron  
 304 Multipliers (CEMs) form a coincidence system for each JNA sector. After hitting the  
 305 start surface, the particle of interest is detected by one CEM (referred to as STOP CEM),  
 306 and the associated secondary electron by a different CEM (referred to as START CEM).  
 307 With this technique, foreground counts can be distinguished from background counts that  
 308 only trigger signals on one CEM at a time, given that background counts on START and

STOP CEMs are not correlated. The expected accidental coincidence countrate, in Jupiter's harsh environment, is  $< 0.4$  count per second.

Despite the optimization to low countrates described above, the spectra in Figure 7 suggests that longer integration times are needed at high energies than at low energies, an important consideration for operations planning and future data analysis. As we did not account for any dissociative processes of the sputtered ENAs, we assume here that  $\text{H}_2$ ,  $\text{O}_2$ , and  $\text{H}_2\text{O}$  are observed and detected by JNA as molecules. In reality, any molecule entering JNA would most likely be dissociated upon encountering JNA's conversion surface (Wieser et al., 2016), as JNA uses a charge conversion surface to ionize ENAs in order to analyze their energy and guide them to JNA's detectors (Kazama et al., 2007). Since dissociated products would each leave the conversion surface with less energy than the original molecule, the assumption that JNA observes molecules likely gives an underestimation of the count rate JNA would measure at low energies.

### 3.5 JNA simulated observation

To illustrate JNA's ability to measure the variability of Jovian plasma precipitation at Ganymede, we calculate the differential ion flux at different latitudes on Ganymede. In Figure 8, the JUICE spacecraft is assumed to orbit Ganymede at an altitude of 490 km (the lowest circular orbit of the nominal JUICE mission) along the  $90^\circ\text{W}$  and  $270^\circ\text{W}$  meridians. At four locations along the orbital track, the flux was averaged over areas corresponding to the size of the footprint of JNA's center pixel. Those areas are referred to as zones. For each zone, the fluxes of sputtered  $\text{H}_2$ ,  $\text{O}_2$ , and  $\text{H}_2\text{O}$  are shown, as well as the JNA one count level for the energy range where JNA can measure. The one count level represents the flux needed for JNA to register 1 coincidence count. It was calculated using JNA's estimated geometric factor, with the assumption that the integration time is 40 seconds (around the time that it would take JNA to move from one JNA projected pixel to the next).

Zone 1 is situated at Ganymede's north pole and covers areas on both the dayside and the nightside. Zone 2 is centered around the sub-solar point. Zone 3 is located along the sub-solar longitude at latitude  $60^\circ\text{N}$ , near the open-closed field-line boundary where the ion flux peaks. Zone 4 is centered around the anti-solar point on the nightside.

Figure 8c shows that the highest flux is observed in Zone 3, reflecting the peak in ion flux at this location near the open-closed field-line boundary where both energetic and thermal plasma have easy access to the surface. The ion population there is dominated by thermal  $\text{O}^+$  (see Poppe et al. (2018) for incident ion flux distributions at different regions on Ganymede). Zone 1, over the north pole, is exposed to an ion population similar to that in Zone 3, although precipitation at the poles is less intense. Consequently, the ENA flux is lower in Zone 1. Zone 2 is centered around the sub-solar point, where the incident ion flux is three orders of magnitude lower than in Zone 3, as Ganymede's magnetic field prevents low energy Jovian plasma from accessing the surface. The ion flux in Zone 2 is therefore dominated by energetic species, which are more efficient at sputtering  $\text{H}_2\text{O}$  than  $\text{H}_2$  and  $\text{O}_2$  (see Figure 3). This explains why the sputtered  $\text{H}_2\text{O}$  flux is about one order higher than that of  $\text{H}_2$  and  $\text{O}_2$ . Figure 8d shows an even larger gap between  $\text{H}_2\text{O}$  fluxes and  $\text{H}_2$  and  $\text{O}_2$  fluxes but there the cause is different. In Zone 4, the ion flux includes contributions of both thermal and energetic species. However, Zone 4 is located on the nightside where the surface temperature is 80 K, which leads to much lower sputtering yields for  $\text{H}_2$  and  $\text{O}_2$  than for  $\text{H}_2\text{O}$ .

In Zone 1 and 3, at the lower end of JNA's energy range (10 eV to 20 eV), sputtered ENA fluxes are high enough to trigger several counts per sector during one pass of JNA over an area as little as little as  $2^\circ$  in latitude. Above 10-20 eV for Zone 1 and 3, and for most of JNA's measuring range for Zone 2 and 4, sputtered fluxes fall below the one count level, implying that longer integration times (i.e., decrease in spatial res-

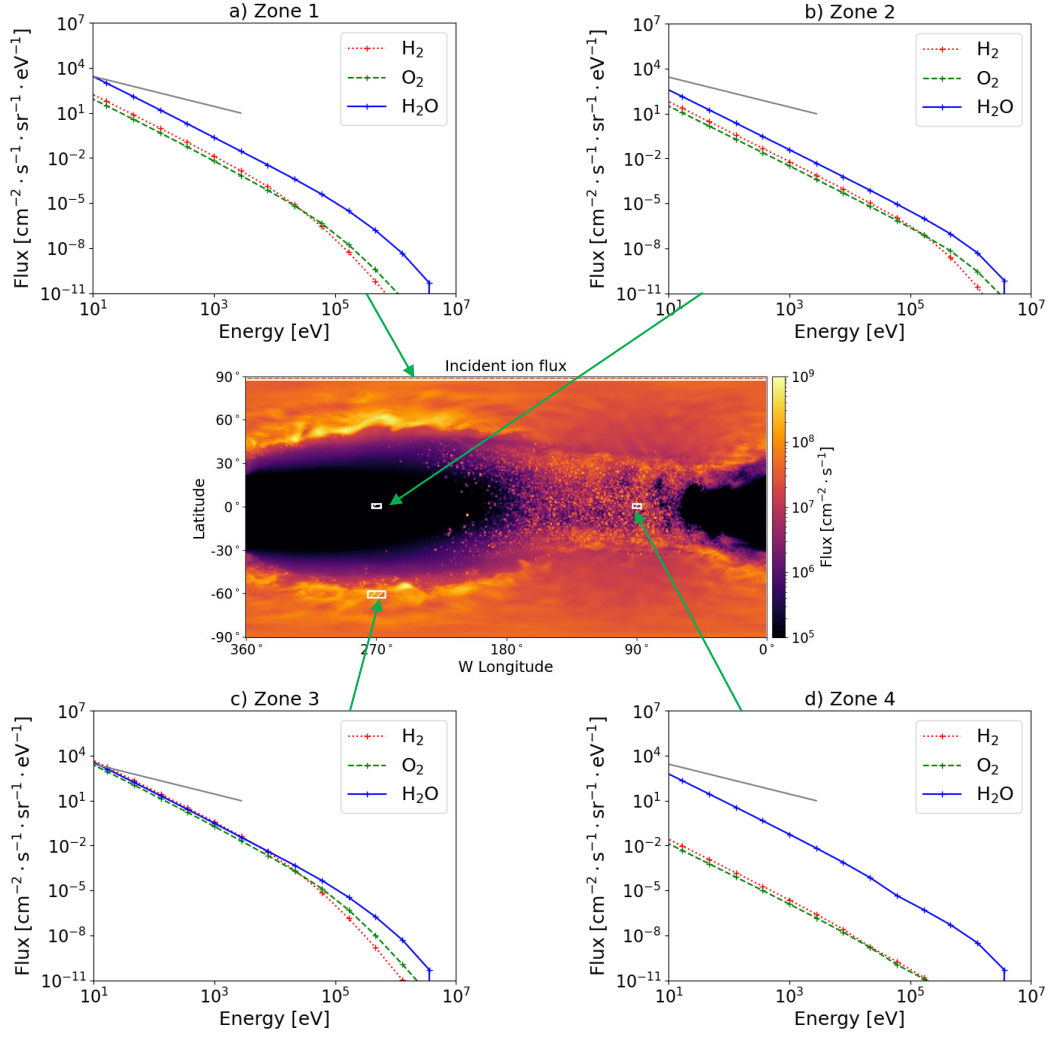


**Figure 8.** Flux of sputtered H<sub>2</sub>, O<sub>2</sub> and H<sub>2</sub>O at four locations on the surface of Ganymede, integrated over incident angles and energies. White rectangles show the area over which the flux was averaged and correspond to the footprint of JNA at 490 km above the surface of Ganymede. The solid gray line indicates the one count level of the JNA instrument for the energy range that JNA can measure (10 eV to 3.3 keV).

360 olution) or repeated observations in similar conditions would be needed. The need for  
 361 longer integration times in Zone 2 and 4 than Zone 1 and 3 will accentuate the effect of  
 362 polar regions being better resolved than equatorial regions, since JUICE will orbit Ganymede  
 363 on a polar orbit that will yield more opportunities to perform measurements over pol-  
 364 lar regions than over equatorial regions.

365 As sputtered fluxes of H<sub>2</sub>O are not temperature-dependent, their variation is a direct  
 366 result of the differences between the incident sputtering populations. We plot them  
 367 together in Figure 9a) for easier comparison. Despite their different ion populations, all  
 368 zones show similar fluxes within one order of magnitude. As expected, the highest fluxes  
 369 are observed over Zone 3 near the open/closed field line boundary while the lowest fluxes  
 370 are seen over Zone 2 and 4. The picture is different for sputtered H<sub>2</sub> and O<sub>2</sub> (Figure 9b

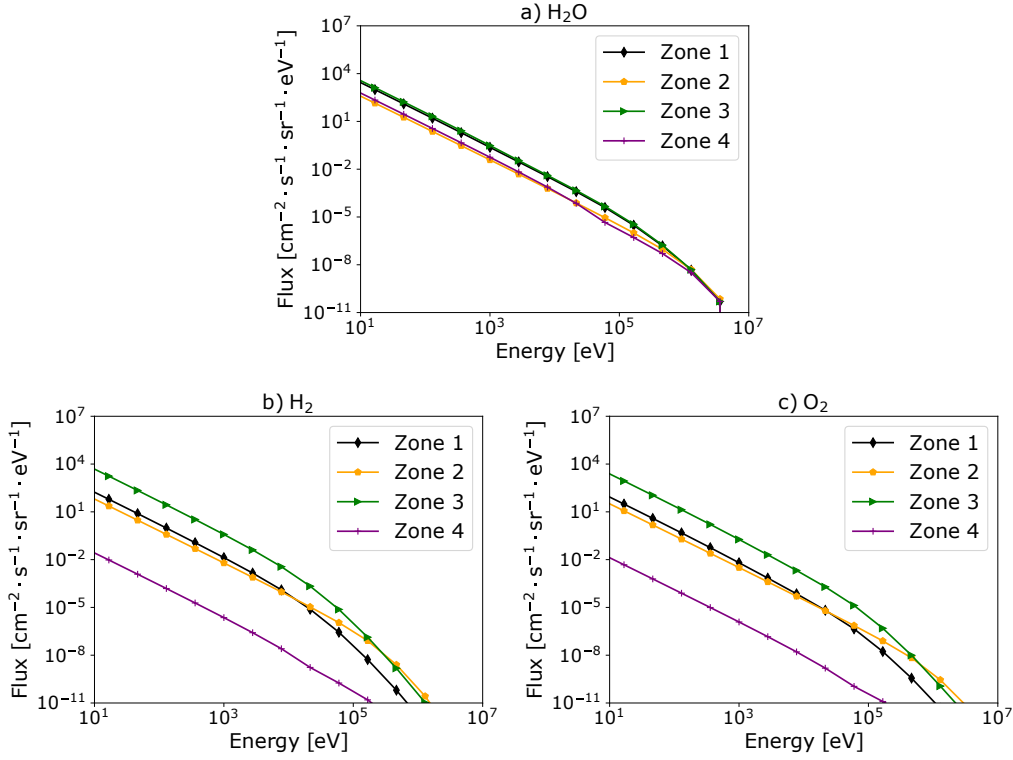


**Figure 9.** Sputtered H<sub>2</sub>O fluxes for all zones, integrated over incident species, energies, and angles.

371 and 9c). There, Zone 4 (on the nightside) shows by far the lowest sputtered fluxes, due  
 372 to the temperature dependence of the sputtering yield of H<sub>2</sub> and O<sub>2</sub>.

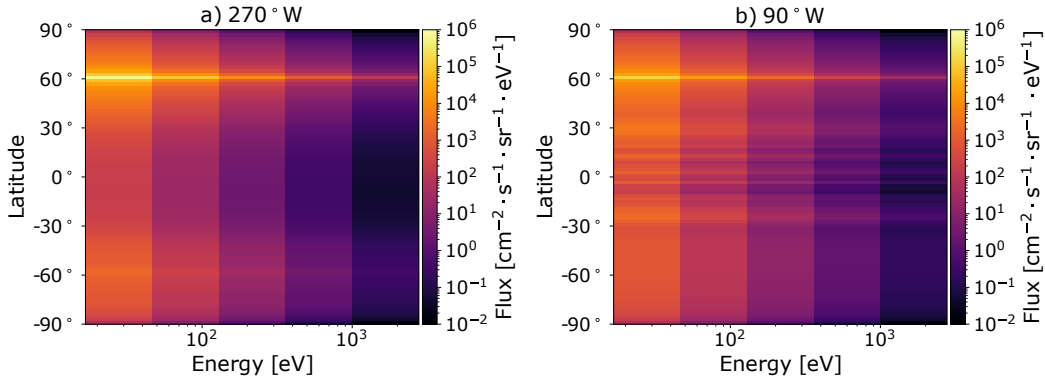


**Figure 10.** Flux of sputtered ENAs integrated over sputtered species and incident species, angles, and energies, shown for each latitude zone corresponding to a JNA footprint along a) 270°W and b) 90°W.

373 In Figure 10, JNA is also assumed to orbit Ganymede at 490 km along the 90°W  
 374 and 270°W meridians but here we divide the orbit track into 120 zones covering 3° each  
 375 in latitude (corresponding to the width of JNA’s center pixel in elevation). The flux for

376 each latitude zone is shown, for the energy range that JNA can measure (between 10 eV  
 377 and 3.3 keV) and integrated over sputtered species and incident species, angles, and en-  
 378 ergies.

379 Generally, Figure 10 shows that the flux of sputtered ENAs varies by about four  
 380 orders of magnitude along the simulated trajectory of JNA for all energy bins in the JNA  
 381 measuring range. Again we observe that the variability of the sputtered neutral flux re-  
 382 flects that of the incident ion flux. Along the 270°W meridian (on the dayside/trailing  
 383 hemisphere), the flux gradually decreases from latitudes  $\pm 60^\circ$  to the equator where the  
 384 flux is minimal and four orders of magnitude lower than at  $+60^\circ$ . We do note that while  
 385 the results from Poppe’s backwards-Liouville tracing model show a significantly higher  
 386 flux at  $+60^\circ$  than at  $-60^\circ$  for the G8 flyby, a significant difference between the north-  
 387 ern and southern hemispheres is not expected in reality.

388 On the 90°W meridian (on the nightside/leading hemisphere), the gradual decrease  
 389 is interrupted at latitudes  $\pm 30^\circ$  by narrow bands of intense sputtering, reflecting the nar-  
 390 row bands of intense ion precipitation in the incident flux (Figure 1). At these latitudes,  
 391 the relative variation between adjacent zones is a factor of two to three. These large lat-  
 392 itudinal variations show that ion precipitation patterns at the surface of Ganymede can  
 393 be retrieved by remotely measuring ENAs.

## 394 4 Discussion

### 395 4.1 Variations along Ganymede’s orbit

396 The ion precipitation distribution used here was simulated to reproduce the plasma  
 397 environment at Ganymede during Galileo’s G8 flyby when Ganymede was at the cen-  
 398 ter of Jupiter’s plasma sheet. Those results are in agreement with recent work by Plainaki  
 399 et al. (2020b), who additionally used MHD simulations to investigate the G2 and G28  
 400 flyby conditions, during which Ganymede was, respectively, above and below the cen-  
 401 ter of the Jovian plasma sheet. Though simulations of sputtered ENA fluxes as a func-  
 402 tion of Ganymede’s orbit are beyond the scope of this paper, Plainaki’s recent work can  
 403 be used together with our results to make a qualitative comment on expected sputtered  
 404 ENA fluxes when Ganymede is above or below the center of Jupiter’s plasma sheet.

405 Results from Plainaki et al. (2020b) show overall decrease of ion precipitation fluxes  
 406 in G2 and G28 conditions compared to G8. Assuming that, as observed in this work for  
 407 the G8 flyby, ENA sputtering patterns are mostly correlated with ion precipitation pat-  
 408 terns for the G2 and G28 cases, then we expect a significant decrease in sputtered ENA  
 409 fluxes when Ganymede is outside the center of Jupiter’s plasma sheet. The leading/trailing  
 410 asymmetry of the precipitating ion flux observed at equatorial regions is a common fea-  
 411 ture of all three scenarios investigated by Plainaki et al. (2020b), so we expect that in-  
 412 tense ENA sputtering in polar regions and in the magnetotail (relative to equatorial re-  
 413 gions) would remain a feature for G2 and G28 conditions as well as for G8 conditions  
 414 investigated in this work. For conditions outside the plasma sheet, Plainaki et al. (2020b)  
 415 point out the existence of ‘shielded areas’ defined as ‘regions with low or zero precipi-  
 416 tation flux’. These shielded areas are large enough for G28 conditions that they create  
 417 a North/South asymmetry, with intense flux to the South and shielding to the North on  
 418 the leading hemisphere, and the reverse situation for the trailing hemisphere. We expect  
 419 this North/South asymmetry to be a feature of sputtered ENA fluxes in G28 conditions  
 420 as it is present for all three species considered by Plainaki et al. (2020b).

### 421 4.2 Energy distribution models

422 In this study we used a Thompson-Sigmund law to calculate the energy spectra of  
 423 sputtered particles. In future work, the backscattering process should also be considered

424 to more accurately simulate the energy spectra of ENAs to be observed at Ganymede.  
 425 Backscattering is another process caused by precipitating ions, in which the impinging  
 426 ion is neutralized (usually) and reflected by the surface. Measurements both in labora-  
 427 tories and in space suggest that backscattered particles would have energies in the range  
 428 that JNA can measure, but distributed according to a Maxwell-Boltzmann-like law rather  
 429 than the Thompson-Sigmund law applicable to sputtering (Futaana et al., 2012; Wieser  
 430 et al., 2016). Backscattering yields are not well modeled, although studies by Wieser et  
 431 al. (2016) and Futaana et al. (2012) suggest that a yield of about 0.1-0.2 can be applied  
 432 for low ( $\sim$ keV) energies. The majority of ENAs in the 10 eV - 1 keV range are produced  
 433 by the sputtering process (by high energy particles), so the backscattered contribution  
 434 to the total ENA spectra is expected to be small. Nevertheless, the different shape of  
 435 their spectra may allow us to distinguish backscattered ENAs from sputtered ENAs.

436 Furthermore, non-linear effects in the sputtering process expected at high energies  
 437 ( $\sim$  10keVs) are not accounted for by the Thompson-Sigmund distribution. Indeed, Thompson-  
 438 Sigmund is based on linear-cascade theory and accurately predicts the experimentally  
 439 measured energy distribution of particles sputtered from various surfaces by projectiles  
 440 with energies of up to 10s of keVs (e.g. Thompson (1968); Haring et al. (1983); Brizzo-  
 441 lara et al. (1988); Goehlich (2001); Samartsev et al. (2005); Wieser et al. (2016)). Mea-  
 442 surements of energy distributions of particles sputtered by  $\sim$ MeV-energy projectiles from  
 443 condensed gases (e.g. Johnson et al. (1983)) only report low-energy sputtered products,  
 444 typically less than 10 eV, perhaps due to limitations of measuring equipment. Conse-  
 445 quently, there currently exists no adequate analytical model available that can accurately  
 446 predict the experimentally measured energy distribution of particles sputtered from con-  
 447 densed gases by  $\sim$ MeV-energy projectiles.

448 For lack of a better model, the Thompson-Sigmund model has therefore been used  
 449 here. Wieser et al. (2016) provides a good argument for the use of Thompson-Sigmund  
 450 in our case as they successfully used it to fit the energy spectra, measured using a JNA  
 451 prototype, of molecules sputtered from water ice under Ganymede surface-like conditions.  
 452 Molecules with energies of up to 1.3 keV were observed under a 33 keV  $O^+$  ion beam  
 453 and followed a Thompson-Sigmund distribution. Thompson-Sigmund was also used in  
 454 previous works to calculate the energy spectra of particles sputtered from airless body  
 455 surfaces such as Mercury (Wurz & Lammer, 2003; Wurz et al., 2010), Europa (Plainaki  
 456 et al., 2010, 2012; Vorburger & Wurz, 2018) and Ganymede (Plainaki et al., 2015), demon-  
 457 strating the need for lab experiments that either validate its use or motivate the devel-  
 458 opment of a better model. In any case, upon deployment in the Jovian environment, JNA  
 459 will provide in-situ experimental energy spectra of atoms sputtered from icy moon sur-  
 460 faces. However, those data will be limited in resolution by the data and power budget  
 461 of the JUICE spacecraft, further demonstrating the need for lab experiments such as those  
 462 mentioned above, performed in controlled and repeatable conditions, to support the anal-  
 463 ysis of JNA data.

### 464 4.3 Angular dependence

465 The angular distribution of sputtered particles has been predicted and measured  
 466 to be  $\cos^f(\theta)$  where  $\theta$  is the angle relative to the surface normal and  $f = 1-2$  depend-  
 467 ing on the target surface (Hofer, 2005). However, most of our results (global sputtering  
 468 rates, sputtering maps, globally averaged energy spectra) are insensitive to the assump-  
 469 tion we used in this work that the particles are sputtered isotropically. Only results relat-  
 470 ing to sputtered particles as observed by JNA would be affected by the isotropic assump-  
 471 tion, but because JNA's field-of-view is small, and the overcosine distribution implies  
 472 preferential sputtering in the direction of JNA (close to zenith), the effect is small  
 473 (factor of 1.5-2).

## 5 Conclusion

We presented a new method to simulate the sputtering process at Ganymede, in order to estimate sputtered ENA fluxes to be observed by the Jovian Neutrals Analyzer, an ENA sensor to be deployed at Ganymede by ESA's upcoming JUICE mission. Our method combines three sputtering yield models to calculate the yield of H<sub>2</sub>, O<sub>2</sub>, and H<sub>2</sub>O separately. Our global sputtering rates show that H<sub>2</sub> and O<sub>2</sub> account for half of the total global sputtering rate from Ganymede. Our total global sputtering rate is in agreement with previous works, but by separating each species we were able to calculate their energy spectra, which is necessary in order to simulate JNA measurements. Indeed, JNA's mass resolution only allows it to distinguish between H and heavier species, but information about the mass and origin of heavier species may be retrieved by looking at their energy spectra. .

We also provided an estimate of expected JNA count rates and simulated the sputtered ENA flux at different locations along the track of a simplified orbit of the JUICE spacecraft. Our results show large latitudinal variations in sputtered ENA flux, demonstrating that JNA will be able to identify ion precipitation patterns by measuring ENAs. Future work will use realistic orbits of the JUICE spacecraft as well as JNA's calibrated instrument response, unavailable at the time of this study.

In conclusion, our results provide insight into the appearance of the data when JNA measures ENAs at Ganymede, as well as how the instrument should be operated optimally under limited power and data budget. The produced sputtering rate maps, energy spectra, and count rates in this study illustrate the capability of the ENA measuring technique to remotely map ion precipitation at Ganymede and provide clues for further potential ENA mapping in other icy bodies. Future work can easily use our model to produce more accurately simulated JNA spectra for different phases of the JUICE mission. Such simulations are crucial for optimizing operations planning and making the most of the limited integration time and data budget.

## Acronyms

**ENA** Energetic Neutral Atoms  
**ESA** European Space Agency  
**JNA** Jovian Neutrals Analyzer  
**JUICE** JUpiter ICy Moon Explorer  
**PEP** Particle Environment Package

## Acknowledgments

A.P. acknowledges support from the Swedish National Space Agency, grant 189/16. S.F. acknowledges support from the Swedish National Space Agency, grant 179/18. A.R.P. acknowledges support from NASA SSW grant #NNX16AR99G. Model results for this work are archived here: [10.5281/zenodo.5607581](https://zenodo.org/record/5607581).

## References

- Allegrini, F., Dayeh, M. A., Desai, M. I., Funsten, H. O., Fuselier, S. A., Janzen, P. H., . . . Wurz, P. (2013, September). Lunar energetic neutral atom (ENA) spectra measured by the interstellar boundary explorer (IBEX). *Planetary and Space Science*, *85*, 232–242. doi: 10.1016/j.pss.2013.06.014
- Barabash, S., Bhardwaj, A., Wieser, M., Sridharan, R., Kurian, T., Varier, S., . . . Wurz, P. (2009, February). Investigation of the solar wind-Moon interaction

- 519 onboard Chandrayaan-1 mission with the SARA experiment. *Current Science*,  
520 *96*, 526–532.
- 521 Baragiola, R., Vidal, R., Svendsen, W., Schou, J., Shi, M., Bahr, D., & Atteberry,  
522 C. (2003, August). Sputtering of water ice. *Nuclear Instruments and Methods*  
523 *in Physics Research Section B: Beam Interactions with Materials and Atoms*,  
524 *209*, 294–303. doi: 10.1016/S0168-583X(02)02052-9
- 525 Brizzolara, R. A., Cooper, C., & Olson, T. K. (1988, November). Energy distri-  
526 butions of neutral atoms sputtered by very low energy heavy ions. *Nuclear*  
527 *Instruments and Methods in Physics Research Section B: Beam Interactions*  
528 *with Materials and Atoms*, *35*(1), 36–42. doi: 10.1016/0168-583X(88)90095-X
- 529 Carnielli, G., Galand, M., Leblanc, F., Modolo, R., Beth, A., & Jia, X. (2020,  
530 November). Simulations of ion sputtering at Ganymede. *Icarus*, *351*, 113918.  
531 doi: 10.1016/j.icarus.2020.113918
- 532 Cassidy, T., Coll, P., Raulin, F., Carlson, R. W., Johnson, R. E., Loeffler, M. J.,  
533 ... Baragiola, R. A. (2010, June). Radiolysis and Photolysis of Icy Satellite  
534 Surfaces: Experiments and Theory. *Space Science Reviews*, *153*(1-4), 299–315.  
535 doi: 10.1007/s11214-009-9625-3
- 536 Cassidy, T., Paranicas, C., Shirley, J., Dalton III, J., Teolis, B., Johnson, R., ...  
537 Hendrix, A. (2013a, March). Magnetospheric ion sputtering and water  
538 ice grain size at Europa. *Planetary and Space Science*, *77*, 64–73. doi:  
539 10.1016/j.pss.2012.07.008
- 540 Cassidy, T., Paranicas, C., Shirley, J., Dalton III, J., Teolis, B., Johnson, R., ...  
541 Hendrix, A. (2013b, March). Magnetospheric ion sputtering and water  
542 ice grain size at Europa. *Planetary and Space Science*, *77*, 64–73. doi:  
543 10.1016/j.pss.2012.07.008
- 544 Cooper, J. (2001, January). Energetic Ion and Electron Irradiation of the Icy  
545 Galilean Satellites. *Icarus*, *149*(1), 133–159. doi: 10.1006/icar.2000.6498
- 546 Famá, M., Shi, J., & Baragiola, R. (2008, January). Sputtering of ice by low-energy  
547 ions. *Surface Science*, *602*(1), 156–161. doi: 10.1016/j.susc.2007.10.002
- 548 Fatemi, S., Poppe, A. R., Khurana, K. K., Holmström, M., & Delory, G. T. (2016).  
549 On the formation of Ganymede’s surface brightness asymmetries: Kinetic sim-  
550 ulations of Ganymede’s magnetosphere. *Geophysical Research Letters*, *43*(10),  
551 4745–4754. doi: 10.1002/2016GL068363
- 552 Futaana, Y., Barabash, S., Grigoriev, A., Winningham, D., Frahm, R., Ya-  
553 mauchi, M., & Lundin, R. (2006, October). Global Response of Mar-  
554 tian Plasma Environment to an Interplanetary Structure: From Ena and  
555 Plasma Observations at Mars. *Space Science Reviews*, *126*(1), 315–332. doi:  
556 10.1007/s11214-006-9026-9
- 557 Futaana, Y., Barabash, S., Wieser, M., Holmström, M., Lue, C., Wurz, P., ...  
558 Asamura, K. (2012, May). Empirical energy spectra of neutralized solar  
559 wind protons from the lunar regolith: EMPIRICAL MODEL OF BACKSCAT-  
560 TERED ENA. *Journal of Geophysical Research: Planets*, *117*(E5), n/a-n/a.  
561 doi: 10.1029/2011JE004019
- 562 Futaana, Y., Barabash, S., Wieser, M., Lue, C., Wurz, P., Vorburger, A., ...  
563 Asamura, K. (2013). Remote energetic neutral atom imaging of electric  
564 potential over a lunar magnetic anomaly. *Geophysical Research Letters*, *40*(2),  
565 262–266. doi: 10.1002/grl.50135
- 566 Galli, A., Vorburger, A., Wurz, P., Cerubini, R., & Tulej, M. (2018, September).  
567 First experimental data of sulphur ions sputtering water ice. *Icarus*, *312*, 1–6.  
568 doi: 10.1016/j.icarus.2018.04.029
- 569 Galli, A., Vorburger, A., Wurz, P., & Tulej, M. (2017, July). Sputtering of wa-  
570 ter ice films: A re-assessment with singly and doubly charged oxygen and  
571 argon ions, molecular oxygen, and electrons. *Icarus*, *291*, 36–45. doi:  
572 10.1016/j.icarus.2017.03.018
- 573 Goehlich, A. (2001, May). Investigation of time-of-flight and energy distributions

- 574 of atoms and molecules sputtered from oxygen-covered metal surfaces by laser-  
 575 aided techniques. *Applied Physics A Materials Science & Processing*, 72(5),  
 576 523–529. doi: 10.1007/s003390100810
- 577 Grundy, W. M., Buie, M. W., Stansberry, J. A., Spencer, J. R., & Schmitt, B.  
 578 (1999). Near-infrared spectra of icy outer solar system surfaces: Remote  
 579 determination of H<sub>2</sub>O ice temperatures. *Icarus*, 142(2), 536–549.
- 580 Gruntman, M. (1997, October). Energetic neutral atom imaging of space plasmas.  
 581 *Review of Scientific Instruments*, 68(10), 3617–3656. doi: 10.1063/1.1148389
- 582 Haring, R., Haring, A., Klein, F., Kummel, A., & De Vries, A. (1983, June). Reac-  
 583 tive sputtering of simple condensed gases by keV heavy ion bombardment. *Nu-  
 584 clear Instruments and Methods in Physics Research*, 211(2-3), 529–533. doi: 10  
 585 .1016/0167-5087(83)90283-1
- 586 Hofer, W. O. (2005). *Angular, energy, and mass distribution of sputtered particles*.  
 587 Berlin, Heidelberg: Springer Berlin Heidelberg. doi: 10.1007/3540534288.16
- 588 Jia, X., Walker, R. J., Kivelson, M. G., Khurana, K. K., & Linker, J. A. (2008,  
 589 June). Three-dimensional MHD simulations of Ganymede’s magnetosphere:  
 590 GANYMEDE MHD SIMULATION. *Journal of Geophysical Research: Space  
 591 Physics*, 113(A6), n/a-n/a. doi: 10.1029/2007JA012748
- 592 Johnson, R. E. (1990). *Energetic Charged-Particle Interactions with Atmospheres  
 593 and Surfaces*. Berlin Heidelberg: Springer-Verlag. doi: 10.1007/978-3-642  
 594 -48375-2
- 595 Johnson, R. E., Boring, J. W., Reimann, C. T., Barton, L. A., Sieveka, E. M., Gar-  
 596 rett, J. W., . . . Lanzerotti, L. J. (1983, September). Plasma ion-induced  
 597 molecular ejection on the Galilean satellites: Energies of ejected molecules.  
 598 *Geophysical Research Letters*, 10(9), 892–895. doi: 10.1029/GL010i009p00892
- 599 Johnson, R. E., Carlson, R. W., Cooper, J. F., Paranicas, C., Moore, M. H., &  
 600 Wong, M. C. (2004). Radiation effects on the surfaces of the Galilean satel-  
 601 lites. *Jupiter: The planet, satellites and magnetosphere*, 485–512.
- 602 Johnson, R. E., Quickenden, T. I., Cooper, P. D., McKinley, A. J., & Freeman,  
 603 C. G. (2003, December). The Production of Oxidants in Europa’s Surface.  
 604 *Astrobiology*, 3(4), 823–850. doi: 10.1089/153110703322736123
- 605 Kazama, Y., Barabash, S., Wieser, M., Asamura, K., & Wurz, P. (2007, Septem-  
 606 ber). Development of an LENA instrument for planetary missions by nu-  
 607 merical simulations. *Planetary and Space Science*, 55(11), 1518–1529. doi:  
 608 10.1016/j.pss.2006.11.027
- 609 Khurana, K., Pappalardo, R., Murphy, N., & Denk, T. (2007, November). The origin  
 610 of Ganymede’s polar caps. *Icarus*, 191(1), 193–202. doi: 10.1016/j.icarus.2007  
 611 .04.022
- 612 Leblanc, F., Oza, A. V., Leclercq, L., Schmidt, C., Cassidy, T., Modolo, R., . . .  
 613 Johnson, R. E. (2017, September). On the orbital variability of Ganymede’s  
 614 atmosphere. *Icarus*, 293, 185–198. doi: 10.1016/j.icarus.2017.04.025
- 615 Marconi, M. (2007, September). A kinetic model of Ganymede’s atmosphere. *Icarus*,  
 616 190(1), 155–174. doi: 10.1016/j.icarus.2007.02.016
- 617 McComas, D. J., Allegrini, F., Bochsler, P., Frisch, P., Funsten, H. O., Gruntman,  
 618 M., . . . Schwadron, N. A. (2009). Lunar backscatter and neutralization of the  
 619 solar wind: First observations of neutral atoms from the Moon. *Geophysical  
 620 Research Letters*, 36(12). doi: 10.1029/2009GL038794
- 621 Orton, G. S., Spencer, J. R., Travis, L. D., Martin, T. Z., & Tamppari, L. K. (1996,  
 622 October). Galileo Photopolarimeter-Radiometer Observations of Jupiter and  
 623 the Galilean Satellites. *Science*, 274(5286), 389–391. doi: 10.1126/science.274  
 624 .5286.389
- 625 Paranicas, C., Cooper, J. F., Garrett, H. B., Johnson, R. E., & Sturmer, S. J. (2009).  
 626 Europa’s Radiation Environment and Its Effects on the Surface. *Europa*,  
 627 Edited by Robert T. Pappalardo, William B. McKinnon, Krishan K. Khurana  
 628 ; with the assistance of René Dotson with 85 collaborating authors. University

- 629 of Arizona Press, Tucson, 2009. *The University of Arizona space science series*  
 630 ISBN: 9780816528448, p.529, 529.
- 631 Plainaki, C., Massetti, S., Jia, X., Mura, A., Milillo, A., Grassi, D., ... Filacchione,  
 632 G. (2020a, September). Kinetic Simulations of the Jovian Energetic Ion  
 633 Circulation around Ganymede. *The Astrophysical Journal*, 900(1), 74. doi:  
 634 10.3847/1538-4357/aba94c
- 635 Plainaki, C., Massetti, S., Jia, X., Mura, A., Milillo, A., Grassi, D., ... Filacchione,  
 636 G. (2020b, September). Kinetic Simulations of the Jovian Energetic Ion  
 637 Circulation around Ganymede. *The Astrophysical Journal*, 900(1), 74. doi:  
 638 10.3847/1538-4357/aba94c
- 639 Plainaki, C., Milillo, A., Massetti, S., Mura, A., Jia, X., Orsini, S., ... Rispoli, R.  
 640 (2015, January). The H<sub>2</sub>O and O<sub>2</sub> exospheres of Ganymede: The result of a  
 641 complex interaction between the jovian magnetospheric ions and the icy moon.  
 642 *Icarus*, 245, 306–319. doi: 10.1016/j.icarus.2014.09.018
- 643 Plainaki, C., Milillo, A., Mura, A., Orsini, S., & Cassidy, T. (2010, November). Neu-  
 644 tral particle release from Europa’s surface. *Icarus*, 210(1), 385–395. doi: 10  
 645 .1016/j.icarus.2010.06.041
- 646 Plainaki, C., Milillo, A., Mura, A., Orsini, S., Massetti, S., & Cassidy, T. (2012,  
 647 April). The role of sputtering and radiolysis in the generation of Europa exo-  
 648 sphere. *Icarus*, 218(2), 956–966. doi: 10.1016/j.icarus.2012.01.023
- 649 Poppe, A. R., Fatemi, S., & Khurana, K. K. (2018, June). Thermal and Energetic  
 650 Ion Dynamics in Ganymede’s Magnetosphere. *Journal of Geophysical Research:*  
 651 *Space Physics*, 123(6), 4614–4637. doi: 10.1029/2018JA025312
- 652 Roelof, E. C. (1987). Energetic neutral atom image of a storm-time ring current.  
 653 *Geophysical Research Letters*, 14(6), 652–655. doi: 10.1029/GL014i006p00652
- 654 Samartsev, A. V., Duvenbeck, A., & Wucher, A. (2005, September). Sputtering of  
 655 indium using Au m projectiles: Transition from linear cascade to spike regime.  
 656 *Physical Review B*, 72(11), 115417. doi: 10.1103/PhysRevB.72.115417
- 657 Shematovich, V. I. (2016, July). Neutral atmosphere near the icy surface of  
 658 Jupiter’s moon Ganymede. *Solar System Research*, 50(4), 262–280. doi:  
 659 10.1134/S0038094616040067
- 660 Shimoyama, Asamura, K., Pontoni, A., Neuland, M. B., Karlsson, S., Wieser, M., ...  
 661 Barabash, S. (2018). Jovian Neutrals Analyzer for the Particle Environment  
 662 Package onboard JUICE. , 2.
- 663 Siscoe, G. L., Eviatar, A., Thorne, R. M., Richardson, J. D., Bagenal, F., & Sul-  
 664 livan, J. D. (1981). Ring current impoundment of the Io plasma torus.  
 665 *Journal of Geophysical Research: Space Physics*, 86(A10), 8480–8484. doi:  
 666 10.1029/JA086iA10p08480
- 667 Siscoe, G. L., & Summers, D. (1981). Centrifugally driven diffusion of iogenic  
 668 plasma. *Journal of Geophysical Research: Space Physics*, 86(A10), 8471–8479.  
 669 doi: 10.1029/JA086iA10p08471
- 670 Teolis, B. D., Plainaki, C., Cassidy, T. A., & Raut, U. (2017, October). Water Ice  
 671 Radiolytic O<sub>2</sub>, H<sub>2</sub>, and H<sub>2</sub>O<sub>2</sub> Yields for Any Projectile Species, Energy, or  
 672 Temperature: A Model for Icy Astrophysical Bodies. *Journal of Geophysical*  
 673 *Research: Planets*, 122(10), 1996–2012. doi: 10.1002/2017JE005285
- 674 Thompson, M. W. (1968, August). II. The energy spectrum of ejected atoms during  
 675 the high energy sputtering of gold. *Philosophical Magazine*, 18(152), 377–414.  
 676 doi: 10.1080/14786436808227358
- 677 Turc, L., Leclercq, L., Leblanc, F., Modolo, R., & Chaufray, J.-Y. (2014, February).  
 678 Modelling Ganymede’s neutral environment: A 3D test-particle simulation.  
 679 *Icarus*, 229, 157–169. doi: 10.1016/j.icarus.2013.11.005
- 680 Vorburget, A., & Wurz, P. (2018, September). Europa’s ice-related atmosphere: The  
 681 sputter contribution. *Icarus*, 311, 135–145. doi: 10.1016/j.icarus.2018.03.022
- 682 Vorburget, A., Wurz, P., Barabash, S., Wieser, M., Futaana, Y., Holmström, M.,  
 683 ... Asamura, K. (2014). First direct observation of sputtered lunar oxy-

- 684 gen. *Journal of Geophysical Research: Space Physics*, 119(2), 709–722. doi:  
685 10.1002/2013JA019207
- 686 Wieser, M., Barabash, S., Futaana, Y., Holmström, M., Bhardwaj, A., Sridharan,  
687 R., . . . Asamura, K. (2009, December). Extremely high reflection of solar wind  
688 protons as neutral hydrogen atoms from regolith in space. *Planetary and Space*  
689 *Science*, 57(14-15), 2132–2134. doi: 10.1016/j.pss.2009.09.012
- 690 Wieser, M., Futaana, Y., Barabash, S., & Wurz, P. (2016, May). Emission of en-  
691 ergetic neutral atoms from water ice under Ganymede surface-like conditions.  
692 *Icarus*, 269, 91–97. doi: 10.1016/j.icarus.2015.12.043
- 693 Wurz, P., & Lammer, H. (2003, July). Monte-Carlo simulation of Mercury’s exo-  
694 sphere. *Icarus*, 164(1), 1–13. doi: 10.1016/S0019-1035(03)00123-4
- 695 Wurz, P., Whitby, J., Rohner, U., Martín-Fernández, J., Lammer, H., & Kolb, C.  
696 (2010, October). Self-consistent modelling of Mercury’s exosphere by sputter-  
697 ing, micro-meteorite impact and photon-stimulated desorption. *Planetary and*  
698 *Space Science*, 58(12), 1599–1616. doi: 10.1016/j.pss.2010.08.003